

- this study do not depend on which waveform was used.
22. It has been assumed that during the EMG burst, muscle is active and generates force but that the cessation of the EMG signal indicates that the muscle is no longer active or generating force. On the basis of this assumption, one would predict that the muscle undergoing the POST conditions would generate negative work because the muscle is lengthening for most of the time the EMG shows activity. However, the time taken for the muscle to activate and the long time taken for relaxation may greatly affect the mechanical performance (5). Hence, when the muscle is actually driven through this in vivo pattern, it generated nearly maximum positive power.
  23. In addition, not having the phase sufficiently negative also reduced the power output. Additional mechanics experiments showed that an increase in strain (from  $\pm 1.5$  to  $\pm 2.5\%$ ) or a shift in phase (back by  $15^\circ$ ) resulted in greater power production.
  24. R. K. Josephson, *J. Exp. Biol.* 147, 533 (1989); J. D. Altringham and I. A. Johnston, *ibid.* 151, 453 (1990).
  25. J. Tang and C. S. Wardle [*ibid.* 166, 33 (1992)] showed that most of the power is generated at the midpoint of the tail sweep in swimming salmon. D. Harper (personal communication) has obtained a similar finding in swimming scup. Superimposition of the tail-tip trace and muscle length change show that all the way back to the caudal peduncle, the muscle is shortening when the tail is sweeping to that side and generating power.
  26. Different species were used in this study than in (3). Although we have no reason to expect important species differences, they cannot be excluded without verification.
  27. The myosepta and skin have alternatively been proposed as transmission elements (4).
  28. The power developed by fish musculature has been approximated in the past from hydrodynamic calculations. These calculations, however, depend on a number of assumptions and the particular model used.
  29. K. Schmidt-Nielsen, *Science* 177, 222 (1972).

Although not having to support body weight would tend to reduce the energetic cost, having to move through a viscous media would tend to increase it. Accurate measures of muscle power will help evaluate the relative importance of the opposing effects.

30. We thank F. Carey and M. Grosenbaugh for advice on data analysis and organizing our stay at the Woods Hole Oceanographic Institution (WHOI); D. Leavitt, B. Lancaster, and B. Tripp for facilitating our work at the Coastal Research Center; M. Moore and B. Woodin for helping us find and maintain scup; D. Harper for advice on fish surgical techniques, for designing a surgical table, and for performing hydrodynamic calculations; R. Golder for illustrating the scup; L. Kerr for advice on image analysis; and F. Thurburg of the Bureau of Marine Fisheries for loaning us the water treadmill. This is WHOI contribution no. 8389. Supported by NIH AR38404 and NSF IBN 9205397.

4 March 1993; accepted 1 June 1993

## Formation of Magnetic Single-Domain Magnetite in Ocean Ridge Basalts with Implications for Sea-Floor Magnetism

Yen-Hong Shau,\* Donald R. Peacor, Eric J. Essene

Although magnetic data are the primary evidence for ocean floor spreading, the processes by which magnetic phases in ocean floor basalts are formed remain poorly constrained. Scanning transmission electron microscopic observations show that magnetic single-domain magnetite in sheeted dike basalts of Deep Sea Drilling Project hole 504B formed through oxidation-exsolution of ilmenite, exsolution of ulvöspinel lamellae, and recrystallization of end-member magnetite by interaction with convecting fluids. The data suggest that the sheeted dike basalts, with single-domain magnetite as an efficient and stable magnetic carrier, contribute significantly to sea-floor magnetism.

Paleomagnetic data from the oceanic crust constitute the primary evidence for sea-floor spreading at mid-ocean ridges (1-3). However, the nature and origin of the magnetic phases responsible for the sea-floor magnetism are not well understood. The primary Fe-Ti oxide mineral in mid-ocean ridge basalts is titanomagnetite, with an ~60 mole percent (mol %) ulvöspinel component ( $Usp_{60}$ ) and a Curie temperature of  $\sim 160^\circ\text{C}$  (4-6). However, magnetization data are generally not consistent with this phase. Rather, the observed magnetic properties (for example, an increase in Curie temperature and a decrease in remanence intensity) of the altered pillow basalts that occupy upper levels of the oceanic crust have been attributed to low-temperature oxidation or maghemitization (4-11). The results of studies of rock magnetism from Deep Sea Drilling Project (DSDP) hole 504B have shown that basalts

from the transition zone and from the sheeted dike complex generally have magnetic properties consistent with end-member magnetite as the magnetic carrier (6, 12, 13). Several mechanisms, such as oxidation-exsolution (14) or low-temperature maghemitization followed by phase inversion, have been proposed to account for the formation of magnetite that presumably exists on a submicroscopic scale (6, 12). Direct characterization of the magnetite with scanning transmission electron microscopy (STEM), scanning electron microscopy (SEM), and electron microprobe analysis is essential to an understanding of the processes by which such magnetite formed.

We used high-resolution STEM (15, 16) to characterize and determine the origin of the iron oxides in basalt from the sheeted dike complex in DSDP hole 504B, located in crust that is 5.9 million years old and  $\sim 200$  km south of the Costa Rica rift. The sample, chosen as representative of a large number studied by other methods, is a massive basalt (sample 107-1; 87 to 90 cm) recovered from the upper part (depth of 870 m within the igneous basement) of the sheeted dike com-

plex during DSDP leg 83. The primary minerals in this basalt have been subjected to hydrothermal alteration that is equivalent to greenschist facies metamorphism (17, 18).

The primary opaque mineral is subhedral to euhedral titanomagnetite that is typically a few hundred micrometers in diameter (Fig. 1). Some titanomagnetite appears to be homogeneous in SEM backscattered electron (BSE) images and in reflected light. Electron microprobe analyses of apparently unaltered parts of titanomagnetite grains give compositions ranging from  $Usp_{61}$  to  $Usp_{74}$ . Some parts of titanomagnetite grains have a mottled texture and are composed of intergrown micrometer-sized sphene and titanomagnetite (Fig. 1). Other areas appear to be homogeneous titanomagnetite, as observed from BSE images, but contain minor Si and Ca, indicative of sphene. In the latter, extremely fine lamellae  $\sim 400$  Å in width are oriented in two directions nearly perpendicular to each oth-

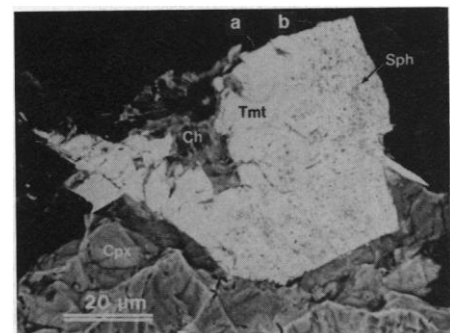


**Fig. 1.** Backscattered electron image of a subhedral titanomagnetite grain (white) showing partial alteration to sphene (gray, mottled texture). The image was taken from an ion-milled specimen prepared for STEM observation. The areas marked a and b are shown in STEM images in Figs. 2 and 3, respectively. Abbreviations: Ch, chlorite; Cpx, clinopyroxene; Sph, sphene; and Tmt, titanomagnetite that appears to be unaltered.

Department of Geological Sciences, University of Michigan, Ann Arbor, MI 48109.

\*Present address: Department of Marine Resources, National Sun Yat-sen University, Kaohsiung 80424, Taiwan, Republic of China.

er (Fig. 2A). Selected area electron diffraction patterns of the host mineral are consistent with that of single-crystal magnetite. The lamellae are oriented parallel to the {100} orientation, as expected for subsolidus exsolution of ulvöspinel from titanomagnetite (19).

An STEM secondary electron image of surface relief demonstrates that the lamellar domains are mostly voids (Fig. 2B). The STEM chemical analyses showed that the host lamellae (dark grey contrast in Fig. 2A) are end-member magnetite ( $U_{sp_0}$ ) (Table 1). Analyses of integrated lamellae (containing host magnetite and empty space) from thin edges give similar Fe contents, but thick areas contain minor amounts of Ti, Si, and Ca (20). Close to the pervasively altered part of a grain of Fe-Ti oxide (area b in Fig. 1), we observe a similar lamellar texture but that consists of host magnetite lamellae and sphene or kassite (Fig. 3, A and B); the sphene has significant Fe and Al contents (Table 1).

The crystallographic relations among the intergrown sphene, kassite, ilmenite, and host magnetite are as follows: The kassite has a preferred orientation with respect to the host magnetite such that {010} of kassite is parallel to {111} in mag-

netite (parallel to sheets of closest packed O atoms in both phases) and  $(100)_{Ks}$  is parallel to  $(110)_{Mt}$ . The ilmenite (with ~10 mol%  $MnTiO_3$ ) (Table 1) has thick lamellae (0.2 to 0.6  $\mu m$ ) oriented parallel to {111} of magnetite (Fig. 3C) as well as small domains coexisting with sphene (Fig. 3B). Some of the thick ilmenite lamellae contain oriented ulvöspinel inclusions, whereas others have been completely replaced by sphene alone or with phyllosilicates. Ilmenite is oriented preferentially, with  $\{001\}_{Im}$  parallel to  $\{111\}_{Mt}$  and  $\langle 120 \rangle_{Im}$  parallel to  $\langle 112 \rangle_{Mt}$ . These relations indicate that the ilmenite lamellae formed in the titanomagnetite through a mechanism of high-temperature oxidation-exsolution (19). Ulvöspinel ( $U_{sp_{-87}}$ , with ~4 mol%  $Mn_2TiO_4$ ) (Table 1) was rarely observed either as relict segments in sphene lamellae or as inclusions that have been partially replaced by sphene in the thick ilmenite lamellae (Fig. 3C). The exact shape and locus of the magnetite-ulvöspinel solvus are not precisely constrained. However, the growth of ulvöspinel lamellae in magnetite with approximately equal amounts of the two phases (Fig. 2) suggests that the titanomagnetite host had a composition of  $U_{sp_{-40-50}}$  (close to the crest of the solvus) before exsolution took place (21-23).

These growth data suggest the following sequence: (i) The oxidation-exsolution of primary titanomagnetite ( $U_{sp_{60-70}}$ ) produced submicroscopic {111} ilmenite lamellae distributed in a host with diminished Ti content. (ii) The pervasive exsolution of {100} ulvöspinel lamellae in the Ti-depleted titanomagnetite host ( $U_{sp_{40-50}}$ ) further decreased the Ti content of the host Ti-bearing magnetite. Both (i) and (ii) likely occurred during the initial cooling of the sheeted dike basalts, although these steps may have occurred during hydrothermal alteration (6). (iii) Ulvöspinel lamellae dissolved, with few left as void space and most replaced by sphene and kassite, whereas the

Ti-bearing magnetite host recrystallized to end-member magnetite during the near-ridge hydrothermal alteration.

Most individual domains of magnetite are 0.03 to 0.1  $\mu m$  across in all dimensions, separated by three mutually orthogonal sets of nonmagnetic phases, or voids, that were once ulvöspinel lamellae. They are thus well within the range of single magnetic domains (24, 25), although the ratios of saturation remanence to saturation magnetization for the sheeted dike basalts at site 504B are more consistent with pseudo-single domain magnetite (6). This discrepancy may be caused by the closely adjacent grains that interact magnetically (6). Facey, Housden, and O'Reilly inferred from saturation magnetization data that the abundance of magnetite is about one-half (by volume) that of titanomagnetite in the sheeted dike basalts from hole 504B (12). This inference is consistent with our observation that approximately one-half of the primary titanomagnetite is now occupied mainly by sphene with some kassite and ilmenite.

The end-member magnetite, the domi-

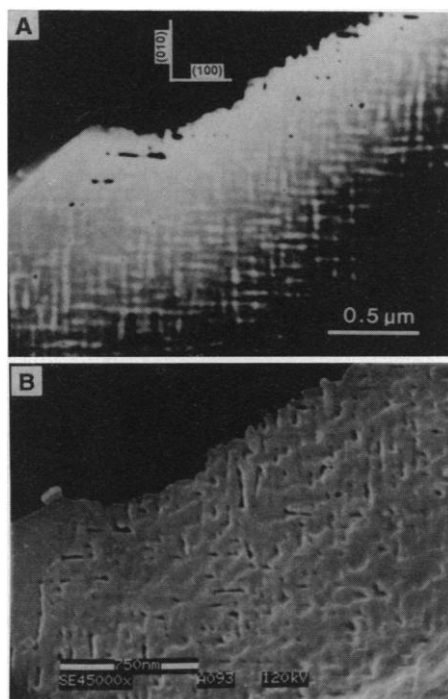


**Fig. 2.** (A) An STEM dark-field image of area a in Fig. 1 showing two sets of lamellae oriented parallel to {100} of titanomagnetite. The inclined boundary (crystal face) to the left of the photograph is parallel to (111). The host lamellae (dark gray contrast) are made up principally of end-member magnetite. (B) An STEM secondary electron image showing surface features from the same area. The elongated voids correspond to the lamellae with a white contrast in (A).

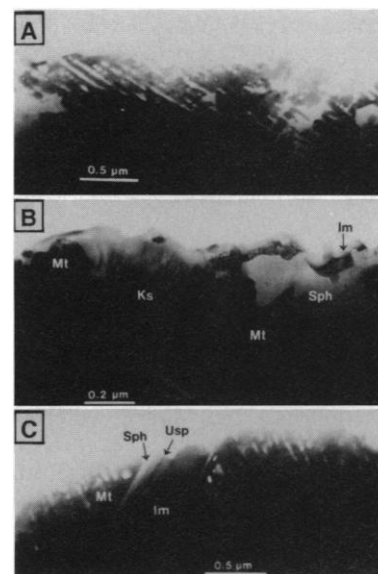


**Fig. 3.** (A) An STEM bright-field image of area b in Fig. 1 showing a lamellar texture that consists of a magnetite framework (black or dark gray) and sphene matrix (white) in two orientations. (B) Transmission beam bright-field image showing intergrown sphene (Sph), kassite (Ks), and ilmenite (Im) in matrix of magnetite (Mt) framework. The elongated ellipse on an ilmenite grain was caused by contamination during STEM chemical analysis. (C) An STEM bright-field image showing a relatively thick ilmenite lamella parallel to (111) and thin sphene lamellae (light gray) parallel to (001) of the magnetite host (dark contrast). The linear traces of the two planes intersect at approximately 65°. Ulvöspinel (Usp) occurs as small segments in the ilmenite lamella and has been partially replaced by sphene (indicated by an arrow).

**Table 1.** Selected STEM chemical analyses of magnetite (Mt), ulvöspinel (Usp), ilmenite (Im), sphene (Sph), and kassite (Ks) (32)

Cation*	Cations per formula unit*				
	Mt	Usp	Im	Sph	Ks
Si	0.17	0.03	0.02	1.00	0.04
Al	0.00	0.00	0.00	0.13	0.06
Ti	0.13	0.92	0.99	0.83	1.91
Fe <sup>2+</sup> †	3.26	1.99	0.86	0.10	0.05
Mn	0.00	0.08	0.09	0.00	0.03
Ca	0.13	0.02	0.03	0.97	0.94
Total	3.69	3.04	1.99	3.03	3.03

\*The cations are defined on the basis of four O for magnetite and ulvöspinel, three O for ilmenite, one Si for sphene, and five O for kassite; each analysis is an average of 2 to 3 point analyses. †Total Fe as Fe<sup>2+</sup>.

nant magnetic carrier in the sheeted dike basalts, did not form simply by oxidation-exsolution, as has commonly been assumed (6, 12, 26). The natural remanent magnetization (NRM) of the sheeted-dike basalts was presumably acquired by the single-domain Ti-bearing magnetite (the host after exsolution) during initial cooling. This was a thermoremanent magnetization (TRM) and was then modified by chemical remanent magnetization of recrystallized end-member magnetite during hydrothermal alteration near the spreading center. The initial cooling and hydrothermal alteration appear to have taken place soon after the intrusion of basalts; therefore, the NRM reflects the original geomagnetic field direction (6).

The thickness of the source layers responsible for the sea-floor magnetic anomalies has long been debated and has been estimated as extending from the uppermost 500 to 1000 m (pillow basalts, layer 2A) of the oceanic crust to depths of ~8 km (essentially the entire oceanic crust) (3, 7, 27, 28). The results of studies of magnetic properties of sheeted dike basalts recovered from DSDP drill holes suggest that the sheeted dike complex (layer 2B) contributes significantly to sea-floor magnetic anomalies (6, 26, 29). However, magnetic data from ocean gabbros indicate that the linear magnetic anomalies originated partly in the gabbro layer (layer 3) (29–31). We have shown that single-domain, end-member magnetite, an efficient and stable carrier of TRM, is responsible for the magnetic properties in the upper levels (depths of ~630 m to at least ~1125 m within the igneous basement) of the sheeted dike complex at site 504B. The resultant NRM intensity of the sheeted dike basalts is on the same order as that of the pillow basalts at site 504B (6, 8, 12). We therefore conclude that the upper sheeted dike basalts from DSDP hole 504B are a significant source of sea-floor magnetic anomalies.

#### REFERENCES AND NOTES

1. F. J. Vine and D. H. Matthews, *Nature* **199**, 947 (1963).
2. F. J. Vine and J. T. Wilson, *Science* **150**, 485 (1965).
3. C. G. A. Harrison, in *The Oceanic Lithosphere*, vol. 7 of *The Sea*, C. Emiliani, Ed. (Wiley, New York, 1981), pp. 219–239.
4. H. P. Johnson and J. M. Hall, *Geophys. J. R. Astron. Soc.* **52**, 45 (1978).
5. N. Petersen, P. Eisenach, U. Bleil, in *Deep Drilling Results in the Atlantic Ocean: Ocean Crust*, M. Talwani, C. G. Harrison, D. E. Hayes, Eds. (American Geophysical Union, Washington, DC, 1979), vol. 2, pp. 169–209.
6. G. M. Smith and S. K. Banerjee, *J. Geophys. Res.* **91**, 10337 (1986).
7. H. P. Johnson and T. Atwater, *Geol. Soc. Am. Bull.* **88**, 637 (1977).
8. T. Furuta, *Init. Rep. Deep Sea Drill. Proj.* **69**, 711 (1983).
9. J. B. O'Donovan and W. O'Reilly, *ibid.*, p. 721.
10. D. M. Pechersky, V. Tikhonov, N. N. Pertsev, *ibid.*, p. 705.
11. G. M. Smith and S. K. Banerjee, *ibid.* **83**, 347 (1985).
12. D. Facey, J. Housden, W. O'Reilly, *ibid.*, p. 339.
13. H. Kinoshita, T. Furuta, H. Kawahata, *ibid.*, p. 331.
14. Oxidation-exsolution is defined as oxidation reactions with oxygen partitioning into titanomagnetite but giving rise to well-oriented lamellar textures that are commonly caused by exsolution.
15. A Philips CM-12 scanning transmission electron microscope equipped with a KeveX (Chesham, United Kingdom) quantum detector was used. The methods for specimen preparation and STEM quantitative chemical analyses are described in (16).
16. Y.-H. Shau, H.-Y. Yang, D. R. Peacor, *Am. Mineral.* **76**, 1205 (1991).
17. J. C. Alt, J. Honnorez, C. Laverne, R. Emmermann, *J. Geophys. Res.* **91**, 10309 (1986).
18. Y.-H. Shau and D. R. Peacor, *Contrib. Mineral. Petrol.* **112**, 119 (1992).
19. S. E. Haggerty, in *Oxide Minerals, Reviews in Mineralogy*, D. Rumble, Ed. (Mineralogical Society of America, Washington, DC, 1976), vol. 3, pp. Hg101–Hg300.
20. The minor amounts of Ti, Si, and Ca cannot account for intimately intergrown sphene and magnetite lamellae in the relatively thick areas. Thus, the lamellar voids also exist in the thick areas; they are real texture and not an artifact caused by ion milling.
21. D. H. Lindsley, *Am. Mineral.* **66**, 759 (1981).
22. G. D. Price, *ibid.*, p. 751.
23. P. P. K. Smith, *ibid.* **65**, 1038 (1980).
24. M. E. Evans and M. L. Wayman, *Can. J. Earth Sci.* **9**, 671 (1972).
25. R. F. Butler and S. K. Banerjee, *J. Geophys. Res.* **80**, 4049 (1975).
26. J. E. Pariso and H. P. Johnson, *ibid.* **96**, 11703 (1991).
27. S. K. Banerjee, *Tectonophysics* **105**, 15 (1984).
28. C. G. A. Harrison, *Annu. Rev. Earth Planet Sci.* **15**, 505 (1987).
29. D. J. Dunlop and M. Prévot, *Geophys. J. R. Astron. Soc.* **69**, 763 (1982).
30. E. Kikawa and K. Ozawa, *Science* **258**, 796 (1992).
31. D. V. Kent, B. M. Honnorez, N. D. Opdyke, P. J. Fox, *Geophys. J. R. Astron. Soc.* **55**, 513 (1978).
32. Analyses were calculated as end-member components (all in mole percent): magnetite, 100% Fe<sub>3</sub>O<sub>4</sub>; ulvöspinel, 86.8% Fe<sub>2</sub>TiO<sub>4</sub>, 9.2% Fe<sub>3</sub>O<sub>4</sub>, and 4.0% Mn<sub>2</sub>TiO<sub>4</sub>; ilmenite, 90.6% FeTiO<sub>3</sub> and 9.4% MnTiO<sub>3</sub>. All components are calculated after subtraction of the Ca, Ti, and Si that were present as a result of contamination by sphene.
33. We thank H. E. Roberson for providing the basalt samples, R. Van der Voo and two anonymous reviewers for comments, and J. C. Alt and D. Suk for many helpful discussions.

26 January 1993; accepted 11 May 1993

## Induction of Apoptosis by the Low-Affinity NGF Receptor

Shahrooz Rabizadeh, Justin Oh, Li-tao Zhong, Jie Yang, Catherine M. Bitler, Larry L. Butcher, Dale E. Bredesen\*

Nerve growth factor (NGF) binding to cellular receptors is required for the survival of some neural cells. In contrast to Trk A, the high-affinity NGF receptor that transduces NGF signals for survival and differentiation, the function of the low-affinity NGF receptor, p75<sup>NGFR</sup>, remains uncertain. Expression of p75<sup>NGFR</sup> induced neural cell death constitutively when p75<sup>NGFR</sup> was unbound; binding by NGF or monoclonal antibody, however, inhibited cell death induced by p75<sup>NGFR</sup>. Thus, expression of p75<sup>NGFR</sup> may explain the dependence of some neural cells on NGF for survival. These findings also suggest that p75<sup>NGFR</sup> has some functional similarities to other members of a superfamily of receptors that include tumor necrosis factor receptors, Fas (Apo-1), and CD40.

Growth factors such as NGF enhance the survival of cells displaying the appropriate receptors. The effects of NGF are mediated at least in part by Trk A, the high-affinity NGF receptor, which is a tyrosine kinase (1). The low-affinity NGF receptor, p75<sup>NGFR</sup>, is a receptor of incompletely characterized function: p75<sup>NGFR</sup> has been shown to increase the affinity of Trk A for NGF (1) and to enhance the specificity of

the Trk family of receptors for neurotrophins (2). p75<sup>NGFR</sup> has some sequence similarity to the tumor necrosis factor receptors [TNFR I (3) and TNFR II (4)], the human cell surface antigen Fas (Apo-1) (5), and the B cell antigen CD40 (6), all of which mediate cell death. In the case of TNFR I and Fas, binding of the receptor by ligand or antibody initiates cell death. In the case of CD40, however, binding by monoclonal antibody (mAb) or ligand inhibits cell death (6). Thus, some cells expressing CD40 are dependent on ligand or mAb binding for survival. Because of structural and functional analogies between the CD40 and p75<sup>NGFR</sup> systems, the possibility that p75<sup>NGFR</sup> serves as a constitutive cell death-promoting molecule that is inhibited by NGF binding was evaluated.

We expressed p75<sup>NGFR</sup> in temperature-

S. Rabizadeh, L. Zhong, J. Yang, Department of Neurology, University of California, Los Angeles, CA 90024.

J. Oh and L. L. Butcher, Department of Psychology, University of California, Los Angeles, CA 90024.

C. M. Bitler, Stanford Research Institute, Menlo Park, CA 94025.

D. E. Bredesen, Department of Neurology and Molecular Biology Institute, University of California, Los Angeles, CA 90024.

\*To whom correspondence should be addressed.